Academic Journal of Science and Technology
ISSN: 2771-3032 | Vol. 9, No. 3, 2024

Abrasive Slurry Jet Characteristics Study

Yang Liu

Xi 'an Shiyou University, Xi 'an, 710065, China

Abstract: In this paper, a coupled computational fluid dynamics-discrete element (CFD-DEM) approach is used to investigate the performance of abrasive slurry jets. Firstly, the CFD method was used to simulate the VES slurry jet flow characteristics. Secondly, an orthogonal design method was used to analyse the sensitivity of the parameters of zero shear viscosity η_0 , relaxation time λ_v and flow index n of the Cross fluid, in which zero shear viscosity η_0 had the most significant effect on the flow field. As the zero-shear viscosity η_0 increases, the velocity of the flow field gradually increases, but the core section of the jet becomes less concentrated and the core section of the jet decreases. Based on the VES fluid formulation used in this project, the optimum zero-shear viscosity, relaxation time and flow index were optimised to 2.5 Pa-s, -0.1s and 0.2 respectively. The results showed that the addition of VES surfactant enhanced the erosion rate of the specimens and that the erosion rate increased with increasing OTAC concentration.

Keywords: VES surfactant; Abrasive jet; Numerical simulation; Particle acceleration.

1. Introduction

Abrasive slurry jetting is a phenomenon that mixes water, abrasives and polymers to improve jet performance, turbulence reduction, energy conversion efficiency and jet speed.[1] . It has been widely used in petroleum, machinery and other fields. Therefore, the addition of certain turbulence reducers to the abrasive water jet is beneficial in improving the jet velocity, core section length, jet set, etc. Minghui W[2] et al. Added polymers to the injection medium to enhance its rock breaking ability.[3] The results showed that the breaking efficiency of the abrasive slurry jet was better than that of the abrasive water jet, and a mathematical model was developed for rock stress under the impact of the abrasive slurry jet, which could reflect the stress distribution of the rock.[4] et al. Investigated the cavitation and bubble collapse phenomena resulting from the addition of drag-reducing polymers to water jets. The coefficients of the viscous and surface tension terms were obtained by fitting the numerical solution to the Rayleigh-Plesset equation, and the Cross model was used to express the shear thinning properties of the polymer solution. The results show that the dispersion of the underwater jet with the addition of a drag reducing agent is small and the cavitation intensity decreases throughout the region but increases in the cavitation area. The bubble collapse process is slower in the drag-reducing solution compared to pure water.

In summary, the study of flow field characteristics in abrasive slurry jets remains of great importance. Most of the slurries in current research are formed by adding polymers to water, while viscoelastic surfactants (VES) change the traditional polymer-to-propellant transport, improve the infusion capacity, have high efficiency, low cost and simple formulation, and they have a broader application prospect than traditional polymers.

2. Numerical Simulation Methods

2.1. Basic structure of the jet stream

When the jet is ejected from the nozzle into the outside area, due to the high speed of the jet, it will immediately mix with the surrounding complex media and produce an exchange of energy and momentum, forming a large velocity difference, which will form a shearing effect on the outer surface of the jet, thus causing the jet speed to decrease rapidly, and the jet will gradually spread, which will also affect the operational efficiency of the abrasive jet.[5] This paper therefore investigates the effect of different nozzle configurations on the operating efficiency of the abrasive jet. This paper therefore investigates the effect of different nozzle structures on the jet efficiency, with the aim of increasing the jet velocity and particle phase velocity and optimising the jet agglomeration, in order to arrive at the optimum nozzle structure parameters. The jet stream is pressurised by a pump and then enters a high pressure line and is ejected through a nozzle to form a high speed jet. After the jet is ejected from the nozzle, if the jet is disturbed by external factors, it will produce certain fluctuations, which will cause the jet boundary to produce local vortices, resulting in a reduction in the main section of the jet, and make the energy carried gradually reduced, the jet nozzle erosion and cutting capacity is reduced. The structure of the water jet is shown in Figure 1[6] P_i is the jet pole, which is the intersection point of the outer boundary of the jet; v_0 is the initial velocity of the jet, m/s; v_x is the velocity of the jet along the axis, m/s; v_y is the velocity of the jet along the radial direction, m/s.

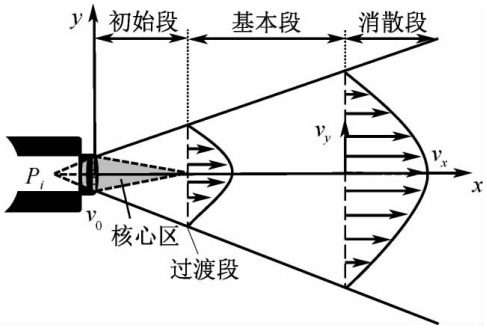

Figure 1. Structure of the water jet

The initial section refers to the core area of the jet where the jet is ejected from the nozzle outlet. When the jet enters the initial section, the surrounding fluid will have some influence on the water jet boundary, resulting in a continuous type of vortex, when the vortex gradually develops into the central region of the jet for the shear layer, the water jet in the shear layer because it is not affected by external media turbulence still maintains the initial speed v_0 ; basic section refers to the development of the jet, the jet is affected by turbulence in the region, also known as the jet fully developed region. Between the initial section and the basic section there is a transition section, which is extremely short. After the transition section, the velocity of the jet axis gradually slows down and the jet begins to spread; the dissipation section is the last section in the jet structure, where a large amount of air is involved in the jet, the jet section is completely mixed with the air medium, the jet is atomised and the dynamic pressure and jet velocity are both very small.

2.2. Control equations

Realizable k-ε[7] The turbulence model is a two-equation model, which is more suitable for jet simulations and provides better computational accuracy than other two-equation models. Equations (2-3) to (2-7) give the control equations for the Realizable k-ε model:

$$\frac{\partial}{\partial t}(\rho k)+\frac{\partial}{\partial x_j}(\rho k \mu_j)=\frac{\partial}{\partial x_j}\left(\left(\mu+\frac{\mu_t}{\sigma_k}\right)\frac{\partial k}{\partial x_j}\right)+G_k-\rho\varepsilon+S_k \quad (3)$$

$$\frac{\partial}{\partial t}(\rho\varepsilon)+\frac{\partial}{\partial x_j}(\rho\varepsilon\mu_j)=\frac{\partial}{\partial x_j}\left(\left(\mu+\frac{\mu_t}{\sigma_\varepsilon}\right)\frac{\partial \varepsilon}{\partial x_j}\right)+\mathrm{C}_1 S\rho\varepsilon-\mathrm{C}_2\rho\frac{\varepsilon^2}{k+\sqrt{v\varepsilon}}+S_\varepsilon \quad (4)$$

$$\mu_t=\rho C_\mu\frac{k^2}{\varepsilon} \quad (5)$$

$$S=\sqrt{2S_{ij}S_{ij}} \quad (6)$$

$$S_{ij}=\frac{1}{2}\left(\frac{\partial u_i}{\partial x_j}+\frac{\partial u_j}{\partial x_i}\right) \quad (7)$$

Where ρ is the fluid density in $\mathrm{kg/m^3}$; x_i and x_j are the respective coordinate components; σ_k and σ_ε are the turbulent Prandtl number for turbulent kinetic energy k and dissipation rate ε ; μ is the fluid viscosity in $\mathrm{Pa\cdot s}$; μ_t is the turbulent viscosity coefficient; C_1 and C_2 are model constants; S is the modulus of the mean strain rate tensor; G_k is the turbulence generated by the mean velocity gradient; S_{ij} is the shear rate tensor; S_k and S_ε are custom source terms.

The solid phase abrasive particles in the abrasive particle jet are calculated using the discrete unit method, where the forces on the abrasive particles in the jet are first analysed and then the trajectory of the abrasive particles is calculated and the position of the abrasive particles is calculated using the integral method. The motion of the abrasive particles in the jet is in the form of translation and rotation, which are related to the combined forces on the abrasive particles, where the combined force is the sum of several component forces on the abrasive particles in the jet, so that the equilibrium state equation of the abrasive is[8] : The

$$m_i\frac{dv_i}{dt}=F_{D,i}+F_{C,i} \quad (9)$$

$$I_i\frac{d\omega_i}{dt}=\sum_{i=1}^{n}T_i \quad (10)$$

Where m is the mass of the particle; v is the particle velocity; I_i is the particle moment of inertia; ω is the angular velocity; $F_{C,i}$ is the particle collision force; $F_{D,i}$ is the particle traction force; and T_i is the particle torque.

$$F_{C,i}=F_{cni}+F_{cti}+F_{Dni}+F_{Dti} \quad (11)$$

Where F_{cni} , F_{cni} , F_{Dni} and F_{Dti} are the normal and tangential contact forces between the particles and the normal and tangential damping forces respectively.

According to the characteristics of the former mixed abrasive jet, the Hertz-Mindlin model, also known as the "elastic-damped-frictional contact mechanics model", is used in this paper and is shown in Figure 2.[9] The diagram is shown in Figure 2.

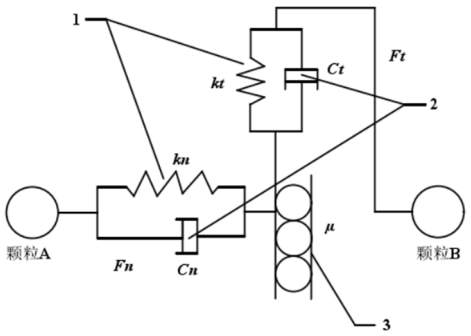

1 - Particle stiffness (spring); 2 - Dampers; 3 - Friction
Figure 2. Contact mechanics model

Normal contact force between particles F_{cni} Can be expressed as

$$F_{cni}=\frac{3}{4}E^*\left(R^*\right)^{1/2}\alpha^{3/2} \quad (12)$$

WhereE^* Denotes the equivalent modulus of elasticity of the particle;R^* Denotes the equivalent radius of the particle.

$$\frac{1}{E^*}=\frac{1-v_1^2}{E_1}+\frac{1-v_2^2}{E_2} \quad (13)$$

$$R^*=\frac{1}{R_1}+\frac{1}{R_2} \quad (14)$$

Where R_1 , E, v_1 correspond to the radius, modulus of elasticity and Poisson's ratio of particle 1, respectively; R_2 , E, v_2 correspond to the radius, modulus of elasticity and Poisson's ratio of particle 2, respectively.

The normal damping force between the particles F_{Dni} can be expressed as

$$F_{Dni}=-2\sqrt{\frac{5}{6}}\beta\sqrt{S_n m^*}v_n^{rel} \quad (15)$$

Where $m*$ is the particle equivalent mass, S_n is the normal stiffness and v_n^{rel} is the normal component of the relative velocity;

The tangential contact force of a particle F_{cti} can be expressed as

$$F_{cti}=-S_t\delta \quad (16)$$

Where δ is the tangential overlap and S_t is the tangential stiffness. The tangential stiffness is taken as follows

$$S_t=R\delta G^*\sqrt{R^*\alpha} \quad (17)$$

Where $G*$ is the equivalent shear modulus of the abrasive particle and is expressed as follows

$$G^*=\frac{2-v_1^2}{G_1}+\frac{2-v_2^2}{G_2} \quad (18)$$

Where G_1 and G_2 are the shear modulus of particle 1 and particle 2 respectively.

The tangential damping force between the particles F_{Dti} can be expressed as

$$F_{Dti}=-2\sqrt{\frac{5}{6}}\beta\sqrt{S_t m^*}\mathrm{v}_t^{rel} \quad (19)$$

Where v_t^{rel} is the tangential component of the relative velocity.

The rolling friction in the simulation is illustrated by the moments on the friction surface, i.e.

$$T_t=-\mu F_{cni}R_t\omega_t \quad (20)$$

Where R_t is the distance from the centre of mass to the point of contact, μ is the rolling friction factor and ω_t is the unit angular velocity vector of the object at the point of contact.

The traction model in the particle control equation uses the following equation

$$F_D=\frac{1}{8}\pi C_D d^2\rho_w\left|V_W-V_P\right|\left(V_W-V_P\right) \quad (21)$$

Where d is the diameter of the particle; V_p is the velocity of the particle; V_W is the velocity of the fluid and C_D is the drag coefficient of the individual particles, the value of which is related to the Reynolds number Re, which is defined in the following equation.

$$R_e=\frac{\rho_w d_p\left|V_w-V_p\right|}{\mu} \quad (22)$$

2.3. Cross fluid principal structure equation

The viscoelastic surfactant solution formed by 1.4% mass fraction of octadecyltrimethylammonium chloride (OTAC) and 0.28% mass fraction of sodium salicylate (nasal) was selected as the abrasive slurry solution, and the apparent viscosity versus shear rate relationship obeyed the Cross principal equation according to the rheological experimental results[10, 11] .

$$\eta=\frac{\eta_0}{1+(\lambda_v\dot{\gamma})^{1-n}} \quad (23)$$

Where η is the apparent viscosity, $\mathrm{Pa\cdot s}$; $\dot{\gamma}$ is the shear rate, $\mathrm{s^{-1}}$; η_0 is the zero shear viscosity, $\mathrm{Pa\cdot s}$; λ_v is the relaxation time, s; and n is the rheological index.

The results of the fit are shown in Figure 2-3 with the fitting parameters: η_0 =2.5 $\mathrm{Pa\cdot s}$, λ_v =0.67s, n=-0.32, and the fit R^2 =0.99.

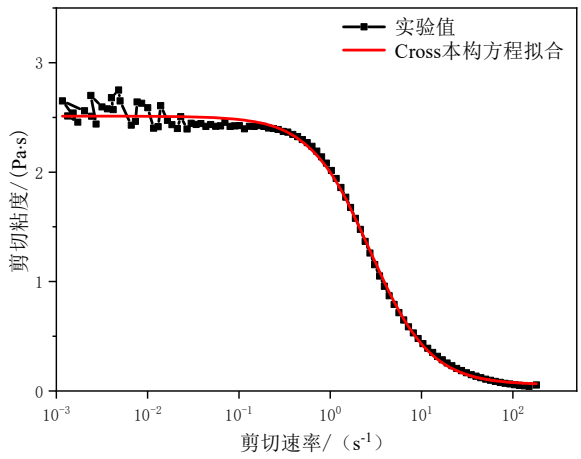

Figure 3. Abrasive slurry rheology curve and Cross instantonal equation fit

2.4. Abrasive model and selection of relevant parameters

The computational fluid dynamics-discrete unit method (CFD-DEM) two-phase coupling method was used to calculate the jet flow field inside and outside the nozzle as well as the particle motion characteristics. The fluids were chosen to be clear water and VES solution for comparison. The flow velocity at the nozzle inlet was 5.5 m/s and the outlet

was set to atmospheric pressure. The abrasive particles in the discrete unit are set as spherical particles of the same size and arbitrarily distributed, with a virtual surface at the nozzle inlet to generate the particles, a time step of 5e-7 s, an abrasive particle size of 0.25 mm and material properties with the following specific parameter settings:

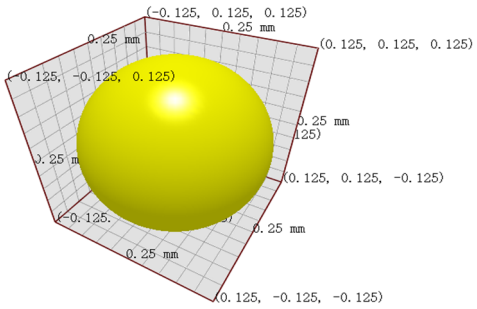

Figure 4. Particle model diagram

1. Material parameter setting

The material parameters of the abrasives and nozzles are shown in Table 1.

Table 1. Material parameter settings

Materials	Poisson's ratio	Shear modulus/Pa	Density (kg/m^3)
Abrasive	0.25	108	2650
Nozzle	0.25	108	

2. Contact parameter setting

The values of the particle-wall and particle-particle contact parameters are given in Table 2.

Table 2. Contact parameters

Collision forms	Recovery factor	Coefficient of static friction	Rolling friction coefficient
Pellets-Pellets	0.5	0.5	0.01
Particle-wall	0.5	0.5	0.01

2.5. Geometric model construction and meshing

As the influence of the abrasive jet nozzle structure parameters on jet fragmentation is mainly determined by the shape of the nozzle flow path as well as the dimensional parameters. The shape of the calculation area is shown in Figure 5. The area for the numerical simulation consists of the inner nozzle area and the outer nozzle jet area, with the specific parameter settings shown in Table 3.

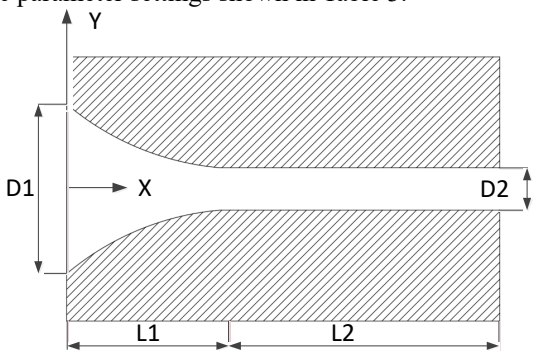

Figure 5. Nozzle geometry

Table 3. Geometric dimensions of the three configurations of nozzles

Nozzle Structure	Inlet internal diameter D1 /mm	Outlet internal diameter D2 /mm	Length of shrinkage section L1 /mm	Taper /(°)	Length of focus section L2 /mm	Total length L/mm
Streamlined	20	5	42.5	45	50	96.5

The mesh division is shown in Figure 6. The selection of the mesh size has an important influence on the simulation results when using DEM software to simulate and calculate the particle motion, the minimum mesh size should be at least 3 times the radius of the abrasive particles. To ensure that the mesh does not affect the simulation results, mesh irrelevance was verified and the three mesh divisions are shown in Table 4.

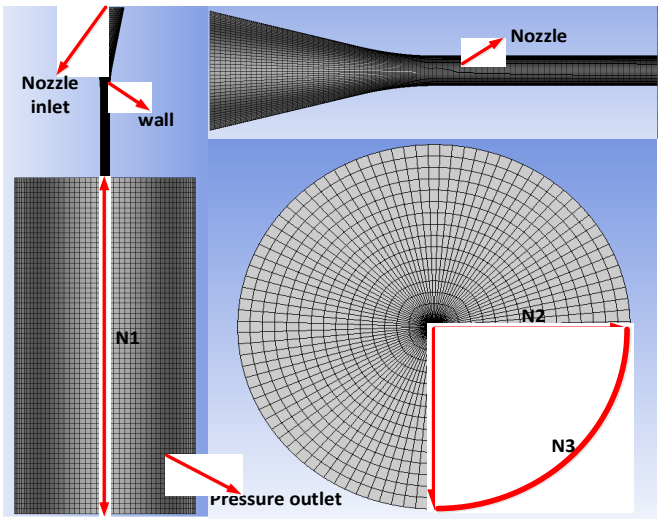

Figure 6. Abrasive jet nozzle calculation grid

Table 4. Grids used for grid-independent studies

Mesh	N1	N2	N3
1	60	29	24
2	90	40	24
3	120	51	24

Three different density grids, mesh-1, mesh-2 and mesh-3, were simulated separately to extract the trend of fluid velocity variation with the position of the median axis. The simulation results are shown in Figure 7, where the three meshes show approximately the same velocity trends. On this basis, mesh-2 was chosen as the grid used for the simulation in order to save computational resources and to have a sufficient number of grids.

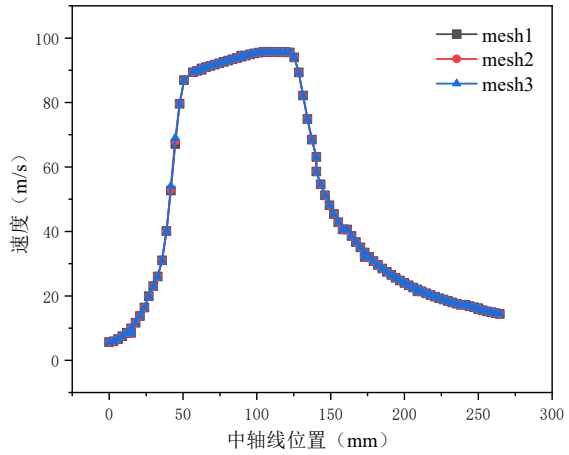

Figure 7. Simulation results of the grid-independence study

3. Analysis of Numerical Simulation Results

3.1. Simulation analysis of the flow field inside and outside the nozzle

Figure 8 shows the velocity distribution of the two solutions, Clear Water and Cross fluid, in the nozzle and in the axial section of the flow field outside the nozzle respectively. Inside the nozzle, the velocity of the jet increases rapidly in the constriction section and remains in the core region of the jet outside the nozzle, after which the velocity begins to decrease. In the area of the jet outside the nozzle, there is an isovelocity core region which gradually dissipates as the axial distance increases and the fluid velocity drops sharply. At the same time, the size of the jet continues to increase and the jet begins to disperse gradually. Comparing the velocity clouds of clear water and Cross fluid in the jet region inside the nozzle with those outside the nozzle, it can be seen that there is a large difference between the Cross fluid and clear water situation due to the shear stress between the pipe wall and the fluid affected by the Cross fluid's own drag reduction capability. Inside the nozzle, the velocity trend of the Cross fluid is approximately the same as that of the clear water, but at a slightly lower velocity. In the jet region outside the nozzle, the drag-reducing effect of the Cross fluid will affect the velocity distribution of this solution, with the Cross fluid showing better agglomeration and the jet spreading relatively far away to carry the particles better. It is clear from the cloud diagram that the Cross fluid is longer in the core region of the jet outside the nozzle and that the fluid velocity decays more slowly.

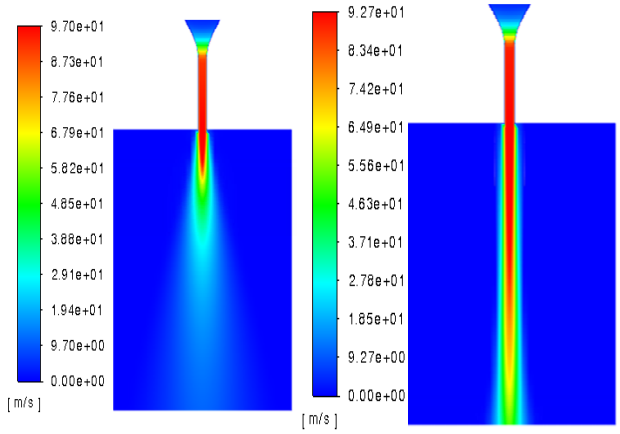

Figure 8. Velocity clouds for different nozzle configurations (inlet velocity 5.5m/s)

Figure 9 is the nozzle inside and outside the flow field axis at the fluid velocity change trend graph, from the graph can be seen in the two fluids inside and outside the nozzle velocity change trend. Inside the nozzle, the fluid flow is always in a state of development, and the flow of clear water at the nozzle outlet basically reaches a steady state, with the velocity of clear water remaining constant. In the jet region outside the nozzle, the jet goes through a short core section before the clear water velocity starts to drop rapidly. In the nozzle shrinkage section, Cross fluid is the first to accelerate, reaching the nozzle focus section, the acceleration trend occurs more reduced, at this time the fluid accelerates slowly. The clear water accelerates more slowly than the Cross fluid in the nozzle constriction section and continues to accelerate as it reaches the nozzle focus section, gradually outpacing the Cross fluid. In the jet area outside the nozzle, the Cross fluid will continue to maintain a high velocity because of its rheological nature.

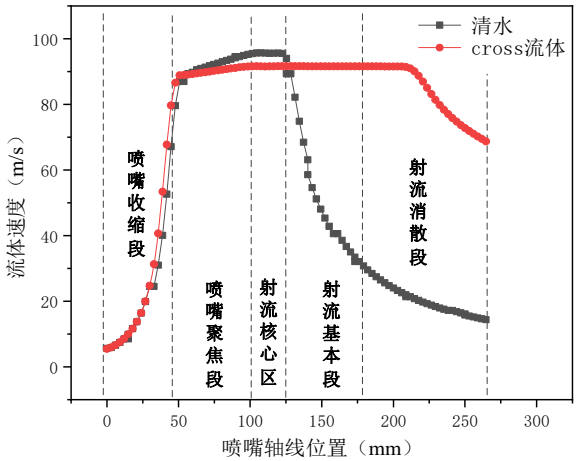

Figure 9. Trend of nozzle mid-axis velocity

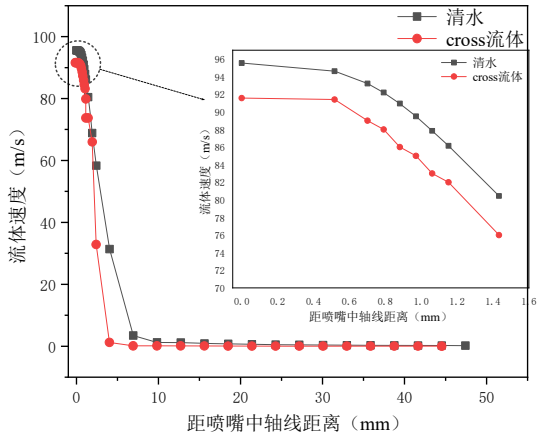

(a) 20mm from the nozzle outlet

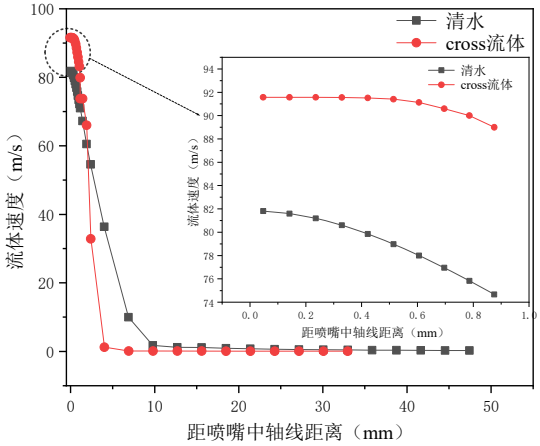

(b) 30mm from the nozzle outlet

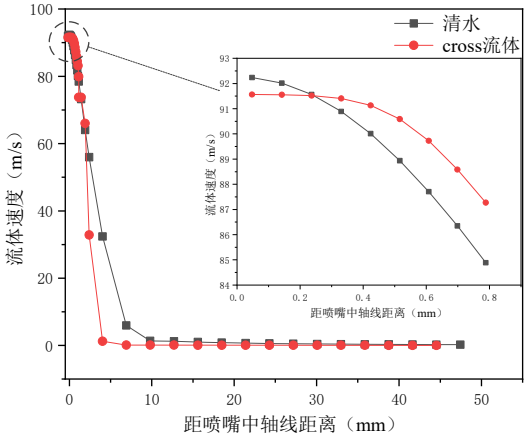

(c) 40mm from the nozzle outlet

Figure 10. Velocity distribution at different spray distance sections

Figure 10 shows the radial distribution of fluid velocity at 20 mm, 30 mm and 40 mm from the nozzle outlet (nozzle inlet velocity was set at 5.5 m/s) for the clear water and Cross fluid solutions respectively. It can be seen that the fluid velocity in the radial direction has a significant change and different spray distance velocity distribution is different, the highest fluid velocity at the centre of the jet, velocity along the radial direction gradually decreases, showing a cusp pattern distribution. Because the jet enters the nozzle outside the jet area, the water jet boundary is affected by the surrounding fluid to form a continuous vortex, the vortex gradually developed to the centre of the jet area for the shear layer, the shear layer of the water jet is not affected by turbulence to maintain the original initial velocity, with the development of the jet, the jet boundary is subject to turbulence, the jet gradually spread, the velocity gradually decreased.

Comparing these two different fluids, it can be seen that at 20mm in the outer jet area, the velocity of the clear water is greater than the velocity of the Cross fluid; at 30mm, the velocity of the clear water and the velocity of the Cross fluid turn around, the velocity of the clear water decreases significantly and the velocity is gradually lower than that of the Cross fluid; at 40mm, the velocity of the clear water is completely lower than the velocity of the Cross fluid.

3.2. Analysis of the particle acceleration mechanism

The trajectory of the abrasive particles in the area inside and outside the nozzle is shown in Fig. 11. The particles are influenced by the fluid motion and in the area of the jet outside the nozzle, the jet spreads gradually and at a decreasing speed, thus driving the abrasive particles to spread in the radial direction. The movement characteristics of the particles in the abrasive jet are influenced not only by the inertial forces present in the abrasive particles themselves, but also by changes in the structure of the jet flow beam. The influence of the fluid properties on the particle velocity can be clearly seen in the particle trajectory, where the abrasive particle velocity increases accordingly in the presence of additives. At the same time, particle aggregation is increased because the additives suppress the creation of vortices in the jet beam, resulting in a more stable and energetically concentrated jet beam.

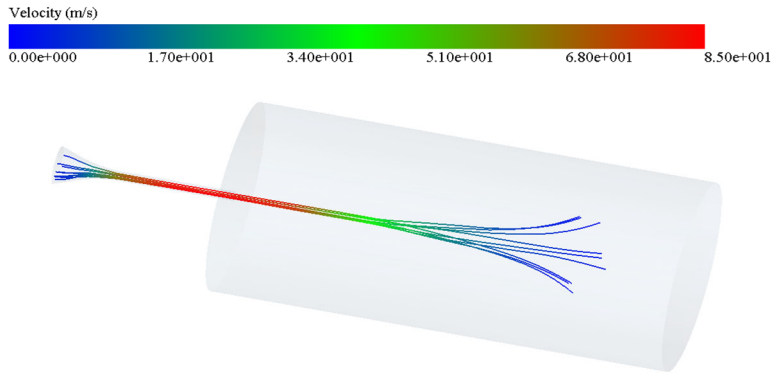

(a) Particles in clear water

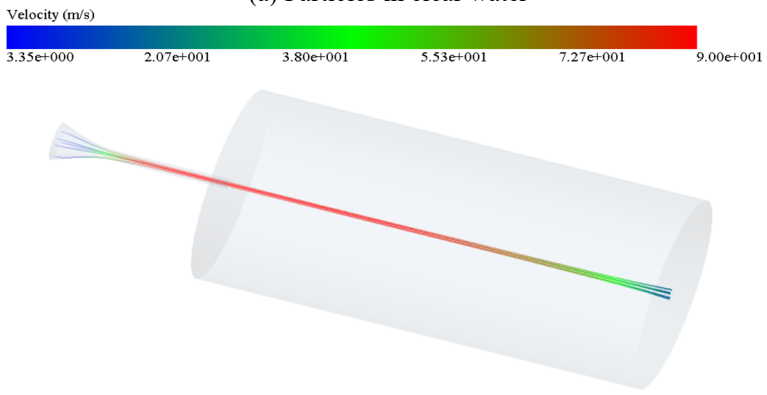

(b) Particles in Cross fluids

Figure 11. Trajectory diagram of particle movement

Figure 12 shows the trend of the velocity of the solid and liquid phases in both fluids with the position of the central axis. It can be seen that the velocity of the fluid and the particles follows approximately the same trend in the nozzle axis. The velocity of both fluids basically reaches its highest value at the nozzle outlet and is able to remain stable. The velocity of the particles in the fluid is in the core of the jet outside the nozzle, and there is still a tendency for the particle velocity to increase under the influence of the inertial forces exerted on the particles as well as gravity. In the basic section of the jet, the jet velocity starts to decrease sharply under the influence of the surrounding medium and gradually spreads in the radial direction.

Nozzle contraction section, abrasive particles and fluid acceleration trend is generally the same, but between the abrasive and fluid due to the existence of the role of speed difference, the fluid speed is always faster than the speed of the particles, with the axis of the distance increases, this speed

difference gradually decreases. In these two different nature of the fluid, the particle velocity there is a process of first acceleration and then deceleration of a process, they are different between the acceleration distance, which is the nature of the Cross fluid decided. As can be seen from Figure 12 (a), the acceleration of the abrasive occurs mainly in the contraction section, when the abrasive starts to enter the focus section, its velocity increases faster, but when the velocity of the abrasive particles increases to a certain level, its velocity increase begins to slow down. The abrasive particles have already reached more than 80% of the fluid velocity by the time they are ejected from the nozzle. In the jet area outside the nozzle, there is still a large slip velocity between the abrasive particles and the fluid. In the out-of-nozzle jet region, the particles are accelerated and reach a maximum velocity during the initial phase of the jet, followed by a deceleration, with the maximum velocity of the abrasive also occurring in the core of the jet. As can be seen in Figure 12 (b), the acceleration trend of the particles in the Cross fluid inside the nozzle is approximately the same as in Clearwater, with a sharp increase in particle velocity in the contraction section and a gradual decrease in acceleration in the focus section. The abrasive particles have reached more than 90% of the fluid velocity by the time they are ejected from the nozzle. In the outer jet region of the nozzle, the particles are still slowly accelerating in the outer jet region under the action of the additives.

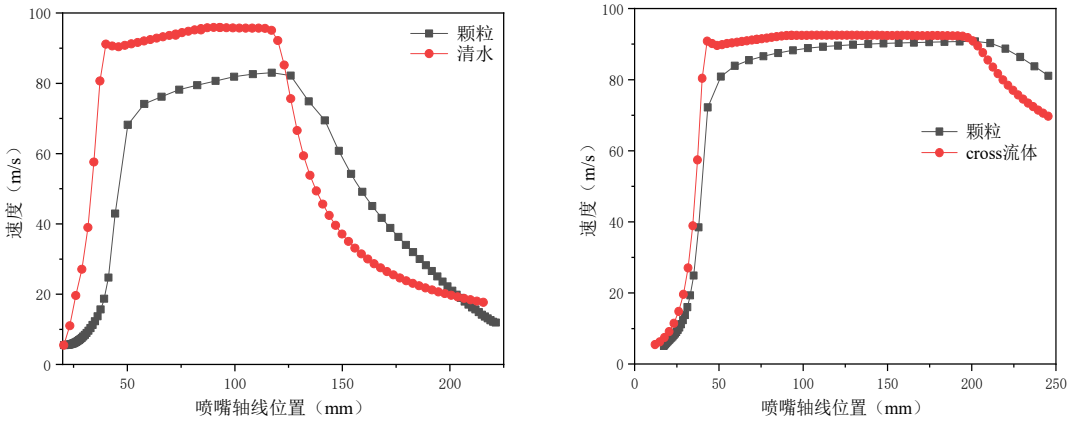

(a) Clear water (b) Cross fluids

Figure 12. Axial distribution of abrasive velocities inside and outside the nozzle

Figure 13 shows the velocity trend of particles in Cross fluid and particles in clear water, by comparing the velocity trend of particles in two different nature fluids with the distance from the axis, it is believed that in the nozzle contraction stage, in the direction of the jet motion in the nozzle axis, the acceleration of the abrasive particles is given by the trailing force of the jet, due to the action of additives, the abrasive slurry jet has a certain drag reducing effect, the more drag reducing effect The more pronounced the drag reduction, the greater the velocity in the core region, which affects the acceleration and distribution of the particles in the jet. The particles in the Cross fluid are the first to start accelerating in the nozzle contraction phase under the effect of the drag reducing agent, i.e. The particles follow each other better and the velocity difference between the fluid and the particles is smaller. In the focusing section the particles continue to follow the fluid and accelerate slowly until the nozzle exit. In the out-of-nozzle jet phase, particles in the Cross fluid still accelerate slowly, maintaining higher velocities to a greater distance on the axis. The velocity of the particles in clear water, on the other hand, has a large velocity slip in the constricted section of the nozzle, and the particles continue to accelerate in the focused section, finally reaching a maximum velocity in the core section of the external jet region, followed by a rapid decrease in velocity. From Table 5 it can be seen that the particle velocity in Cross fluid increases by about 8% compared to the particle velocity in clear water.

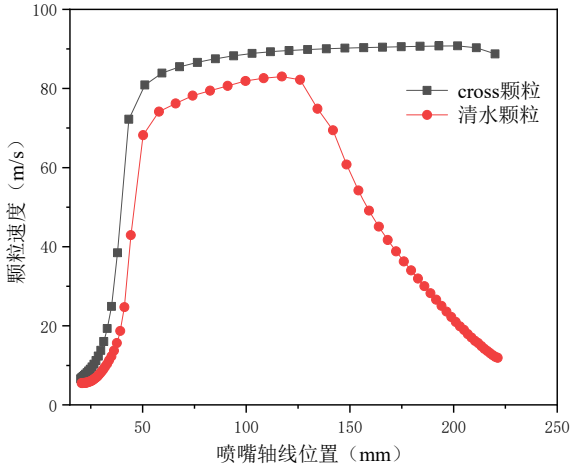

Figure 13. Comparison of particle velocity distribution curves

Table 5. Velocities of particles corresponding to partial positions on the axis

On the nozzle axis Position/mm	Particles in clear water Speed/ms-1	Particles in Cross fluids Speed/ms-1	Speed difference ratio/%
58.6424	74.1433	83.9088	11.64%
66.89575	76.1993	85.4928	10.87%
75.3076	78.1792	86.6006	9.72%
83.852	79.4703	87.5065	9.18%
92.5008	80.6659	88.2665	8.61%
101.24045	81.9033	88.8673	7.84%
110.058	82.5969	89.2869	7.49%
118.922	83.0100	89.6003	7.36%
127.801	82.1923	89.8456	8.52%

3.3. Optimisation of rheological parameters of abrasive slurries based on orthogonal tests

Based on the numerical simulation optimization results, it was concluded that the addition of a drag reducing agent resulted in a good aggregation effect of the jet, a greater concentration of energy and a greater acceleration of the particles, however, based on the numerical simulation only the superiority of the abrasive slurry jet was determined, and the best rheological parameters were not selected from it. Therefore, in order to obtain a reasonable rheological parameter, the higher the nozzle exit end velocity, the better the jet performance is considered, considering its index of the cutting nozzle exit initial velocity. The Cross fluid instantonal equation was used as the basis to vary the zero shear viscosity η_0 , the flow index n , and the relaxation time λ_v , respectively, to investigate the effect of the rheological parameters on the flow field inside and outside the streamlined nozzle.

According to the above simulation results, the structure of the abrasive slurry jet nozzle was chosen as a streamlined nozzle with an inlet inner diameter of 20 mm, an outlet inner diameter of 5 mm, a contraction section length of 42.5 mm, a taper of 45°, a focus section length of 50 mm and a total length of 96.5 mm. The rheological parameters of the abrasive slurry were fixed at $n=-0.2$, $\lambda_v=0.9$ and the zero shear viscosity was changed at η_0 to simulate the flow field inside and outside the nozzle. η_0 was taken as 1.5, 2.0 and 2.5 respectively. As shown in Figure 14, it can be seen that as the zero shear viscosity η_0 increases, the velocity of the flow field gradually increases, but the jet agglomeration becomes worse and the core section of the jet decreases.

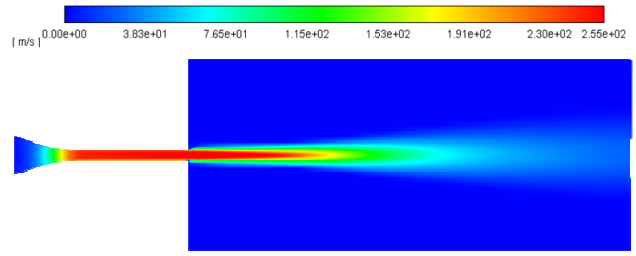

(a) η_0 =2.5 , n=-0.2, λ_v =0.9

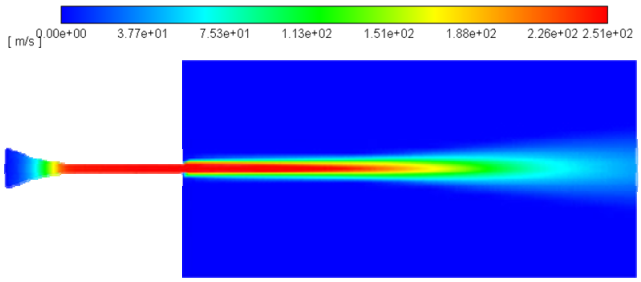

(b) η_0 = 2.0, n = -0.2, λ_v = 0.9

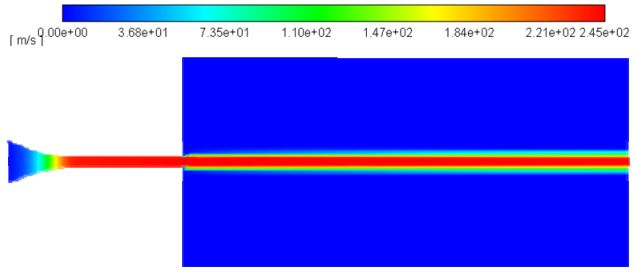

(c) η_0 = 1.5, n = -0.2, λ_v = 0.9

Figure 14. Different η_0 cloud of velocity variations inside and outside the nozzle

Figure 15 shows the variation law of abrasive particle velocity along its trajectory in the abrasive slurry jet at different zero shear viscosities η_0 , and to effectively describe the velocity difference, the inlet velocity is taken as a constant value of 15 m/s. It can be seen that the variation law of abrasive particle velocity at different rheological parameters, where the particle movement law is influenced by the fluid properties, increases with the zero shear viscosity η_0 , the velocity of abrasive particles increases accordingly, and the particle The sharp increase in velocity also occurs in the shrinkage phase, and unlike the slurry, there is still a large upward trend in particle velocity after entering the focusing section.

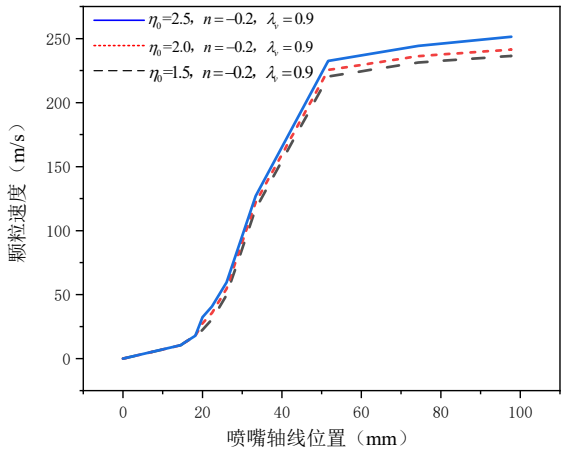

Figure 15. Variation of abrasive particle velocity at different η_0

3.4. Orthogonal experimental design

The orthogonal design is a commonly used experimental design method. The rheological parameters were selected as zero shear viscosity η_0 for l.5 Pa-s, 2.0 Pa-s, 2.5 Pa-s, flow index n for -0.05, -0.1, -0.2 and relaxation time λ_v for 0.2s, 0.3s, 0.9s. On this basis, the different rheological parameters were optimised to obtain a better jet impact The effect of the rheological parameters was optimised to obtain a better jet impact. The other experimental factors were selected according to the results of the initial optimisation of the numerical simulation. The orthogonal factors are shown in Table 6.

Table 6. Table of orthogonal factors

Level	Shear viscosity η_0/Pa·s	Flow index n	Relaxation time / λ_v s
1	1.5	-0.05	0.2
2	2.0	-0.1	0.3
3	2.5	-0.2	0.9

(1) Experimental programme

Based on the selected factors and levels, the simulation experiments can be arranged. The specific experimental protocols arranged are shown in Table 7 Orthogonal experimental design protocols

Table 7. Orthogonal experimental design scheme

Number of experiments	Shear viscosity η_0/Pa·s	Flow index n	Relaxation time / λ_v s
Experiment 1	1.5	-0.2	0.9
Experiment 2	1.5	-0.1	0.3
Experiment 3	1.5	-0.05	0.2
Experiment 4	2.0	-0.2	0.3
Experiment 5	2.0	-0.1	0.2
Experiment 6	2.0	-0.05	0.9
Experiment 7	2.5	-0.2	0.2
Experiment 8	2.5	-0.1	0.9
Experiment 9	2.5	-0.05	0.3

(2) Based on the orthogonal experimental design Table 7, the exit velocity of the jet medium under different rheological parameters as shown in Table 8 was obtained by simulating and analyzing the rheological parameters affecting the jet effect

Table 8. Fluid velocity at nozzle outlet

Number of experiments	Zero shear viscosity η_0/Pa·s	Flow index n	Relaxation time λ_v/s	Nozzle exit speed m·s^{-1}
Experiment 1	1.5	-0.2	0.9	245
Experiment 2	1.5	-0.1	0.3	251
Experiment 3	1.5	-0.05	0.2	260
Experiment 4	2.0	-0.2	0.3	248
Experiment 5	2.0	-0.1	0.2	256
Experiment 6	2.0	-0.05	0.9	256
Experiment 7	2.5	-0.2	0.2	252
Experiment 8	2.5	-0.1	0.9	255
Experiment 9	2.5	-0.05	0.3	262
K1	252	248.333	252	
K2	253.333	254	253.667	
K3	256.333	259.333	256	
R	4.333	11	4	

3.5. Analysis of orthogonal results

The analysis of variance (ANOVA) was conducted from the variance of the observed variables to investigate which of the many control variables were the ones that had a significant effect on the observed variables, and the results of the

experiment were analysed for variance, resulting in ANOVA Table 9.

Table 9. Analysis of variance table

Source	Square and	Freedom	Mean Square	F-value	Significance
Shear viscosity					
Flow index	120.222	2	60.111	1.797	*
Relaxation time	48.222	2	24.111	0.721	
λ_v	3.556	2	1.778	0.053	
Error	66.889	2	33.444		
Total after amendment	238.889	8			

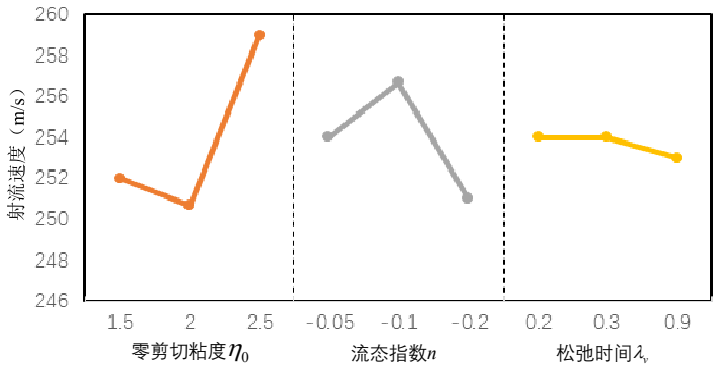

Figure 16. Curve effect diagram

The curve effect Figure 16 shows that of the three rheological parameters, the zero shear viscosity η_0 has a greater effect on the flow rate at the nozzle outlet, followed by the flow index, but neither varies linearly. At a zero shear viscosity η_0 of 2.5 Pa-s and a flow index n of -0.1, the abrasive slurry velocity is optimal at the nozzle, while for the relaxation time λ_v the abrasive slurry jet decreases at the nozzle outlet with increasing relaxation time λ_v and varies linearly.

Table 10. Table of optimal rheological parameters in the abrasive slurry jet

Shear viscosity η_0 /Pa·s	Flow index n	Relaxation time / λ_v s
2.5	-0.1	0.2/0.3

4. Experimental Study of Abrasive Slurry Nozzle Erosion

4.1. Experimental preparation

4.1.1. Preparation of the solution

The reagents used in the preparation of VES solution were octadecyltrimethylammonium chloride (OTAC), isopropanol, sodium salicylate (nasal) and deionised water. The OTAC master solution was firstly prepared using a mass fraction of 60% OTAC with 20% distilled water and 20% isopropanol by stirring and heating before the experiment. 0.2%, 0.5% and 0.7% mass of OTAC master solution was taken and nasal counter ionic salt was added in the proportion of 0.04%, 0.1% and 0.14% respectively to configure the VES solutions with different OTAC concentrations using A stirrer was used for a further 30min. Before each test, the solution was left to stand for more than 24 hours to ensure that there were no air bubbles in the solution at the time of measurement and the experiment could be carried out.

4.1.2. Experimental materials

The specimens used for the abrasive slurry jet nozzle erosion experiments were 304 stainless steel, the chemical composition of which is shown in Table 11. 304 stainless steel was made into a 40mm x 40mm square specimen, and the specimens were sandpapered to a bright surface finish. The solid phase particles in the two-phase flow used for the experiments were selected from 20 to 40 mesh quartz sand, the quartz sand particles SEM image is shown in Figure 17, the solution was water with different OTAC concentration of VES solution.

Table 11. 304 stainless steel composition table

C (%)	Si (%)	Mn (%)	Cr (%)	Ni (%)	S (%)	P (%)
≦ 0.08	≦1.0	≦2.0	18.0 - 20.0	8.0 - 10.0	≦ 0.03	≦ 0.045

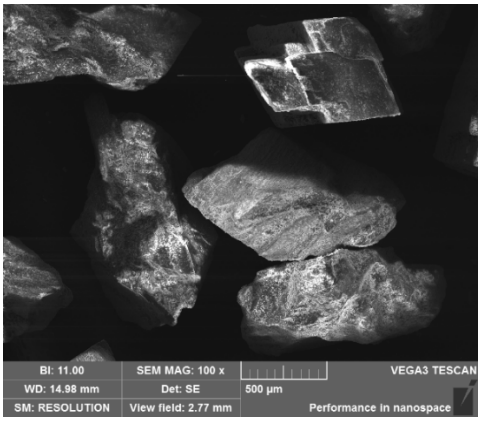

Figure 17. Scanning electron micrograph of quartz sand used in the erosion experiments

4.1.3. Experimental design

The principle of the nozzle erosion experiment is shown in Figure 18, the experimental device to take a circular flooding type, by the air compressor, pneumatic diaphragm pump, flow meter, stirring device, specimen clamping device, pipeline composition, where the pneumatic diaphragm pump relies on the air compressor driven, stirring device can achieve uniformity of abrasive particles in the solution. The specimens used for the experiments were 304 stainless steel, which were machined and polished to a smooth finish in order to observe the erosion results. Finally, the specimens were weighed using an electronic balance scale, and the prepared water, VES solution, of which the VES solution was taken in three formulations, 0.2% OTAC with 0.04% nasal, 0.5% OTAC with 0.1% nasal, and 0.7% OTAC with Quartz sand with a mass fraction of 2% was added to the solutions to be tested and mixed to form an abrasive slurry, and the equipped solutions were poured into the experimental apparatus. After the solution has been prepared, the treated specimen is mounted in the experimental clamping device with the distance between the specimen and the nozzle fixed at 18 mm. After starting the stirring device to mix the solution with the quartz sand, the air compressor is switched on and the experiment is started.

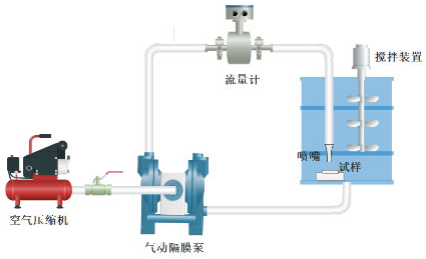

Figure 18. Schematic diagram of the erosion experimental setup

Fig. 19 shows a real colour confocal microscope. The surface morphology of the specimen changes considerably after the erosion test, so a real colour confocal microscope is used to scan the specimen after the erosion test to analyse the changes in the surface morphology of the specimen from a microscopic point of view. The microscope works by converging the light beam from the light source on the specimen through the incident pinhole, beam splitter and objective lens. 15 frames/second is the scanning speed of the HYBRID, which is four times faster than the general confocal microscope, enabling high-speed automatic measurement, image stitching and high-speed camera observation. As a result, the true colour confocal microscope is able to accurately measure the surface morphology of the specimen crater after the erosion experiment.

Figure 19. True colour confocal microscope

4.1.4. Calculation of erosion rates

The rate of erosion is measured using the weight loss method, which mainly calculates the mass loss per kilogram of sand to the specimen, therefore the rate of erosion is calculated using kg/kg as the unit and the following formula is used for the calculation:

$$ER(\frac{\text{kg}}{\text{kg}})=\frac{\text{材料质量损失(kg)}}{\text{流过材料表面的总砂量(kg)}}=\frac{(m_0-m_1)}{M_{sand}gt} \quad (24)$$

Where m_0 is the mass of the specimen before erosion, g; m_1 is the mass of the specimen after erosion, g; ER is the erosion rate, kg/kg; M_{sand} is the sand mass flow rate, kg/s; t is the erosion wear test time, s.

4.2. Experimental results

4.2.1. Nozzle erosion experimental results

According to the above circulating submerged experimental design, the optimized streamline nozzle was used to carry out corrosion experiments on the 304 stainless steel specimens, and the corrosion rates of the specimens were calculated from the experimental measurement data at different concentrations of OTAC solution as shown in Figure 20. It can be seen that when the experimental solution is chosen from water, the corrosion rate of the specimen is the lowest, after adding 0.2% OTAC and 0.04% nasal additives to the water, the corrosion rate increases significantly, from 1.9 x 10-7 kg/kg to 3.2 x 10-7 kg/kg, the corrosion rate increases by 75%, it can be seen that under the action of VES solution, the abrasive jet on the specimen's The abrasive jet under the effect of VES solution significantly enhanced the erosion rate of the specimen. The VES solution ratio was then changed and two different concentrations of 0.5% OTAC and 0.7% OTAC were added to the water to form the abrasive slurry solution. Comparing the corrosion rates of 304 stainless steel specimens with the different VES solution ratios, it can be seen that as the OTAC concentration increases, the corrosion rate of the specimens increases.

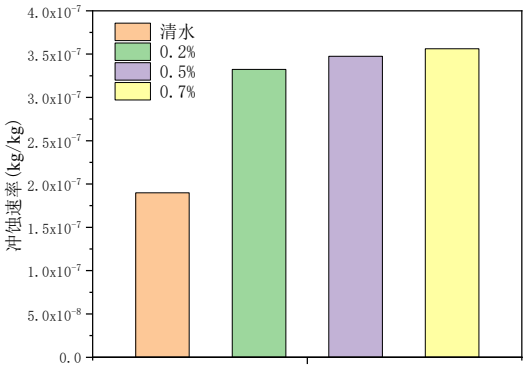

Figure 20. Purging rate of specimens with different concentrations of OTAC solution

4.2.2. Experimental results of erosion profile scanning

Figure 21 shows the specimens after 3 hours of etching with water and VES solution respectively. It can be seen that the pits are deeper in the VES solution etched specimens compared to the water etched specimens, this is due to the turbulent flow reduction effect of the VES slurry solution, which enables the abrasive particles in the abrasive jet to travel at a faster rate. It can be clearly observed that the crater area of the specimen after VES solution erosion is smaller, with a crater diameter of 5mm, while the crater area of water erosion is larger, with a crater diameter of 7.5mm. Figure 22 shows the percentage of particles at the centre of the jet, the

VES solution has a strong aggregation to the jet, so at the nozzle centre axis, the percentage of particles in the VES solution is always higher than the percentage of particles in water, i.e. VES solution as an abrasive jet carrying fluid can effectively increase the fluid and particle agglomeration.

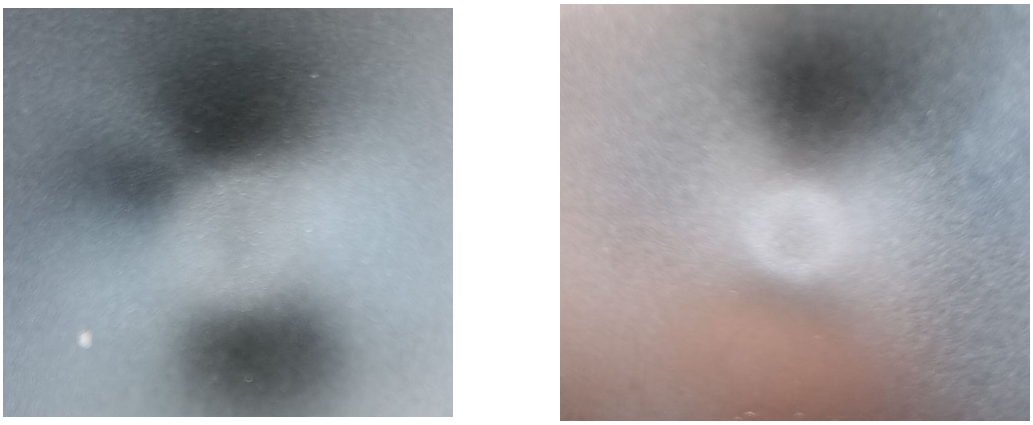

(a) Clear water (b) VES solution

Figure 21. Physical view of specimen after 3 hours of erosion

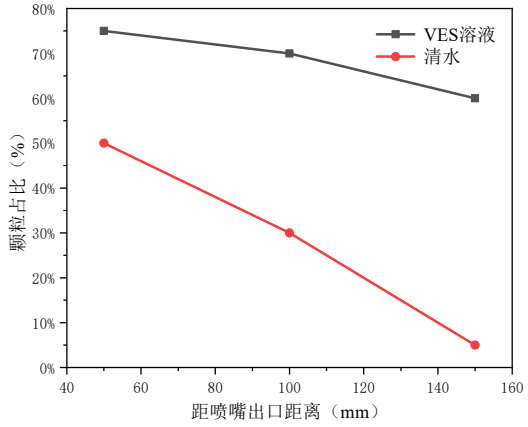

Figure 22. Percentage of particles at the centre of the jet at different spray distances

Figure 23 shows the surface morphology of the 304 stainless steel specimen before and after abrasion, using an optimised streamlined nozzle structure with a fixed distance of 18 mm between the nozzle and the specimen, which shows that the surface of the un-etching specimen has a smooth shape, while after abrasive slurry jet abrasion the morphology exhibits an uneven shape. Figure 24 shows the trend of particle velocity at the nozzle axis. The particle velocity in the VES solution is always higher than that of the particles in clear water due to the turbulent flow reduction effect of the VES surfactant, i.e. The addition of the VES additive makes the velocity slip of the solid-liquid two-phase flow smaller, the particle following performance stronger and the erosion rate higher.

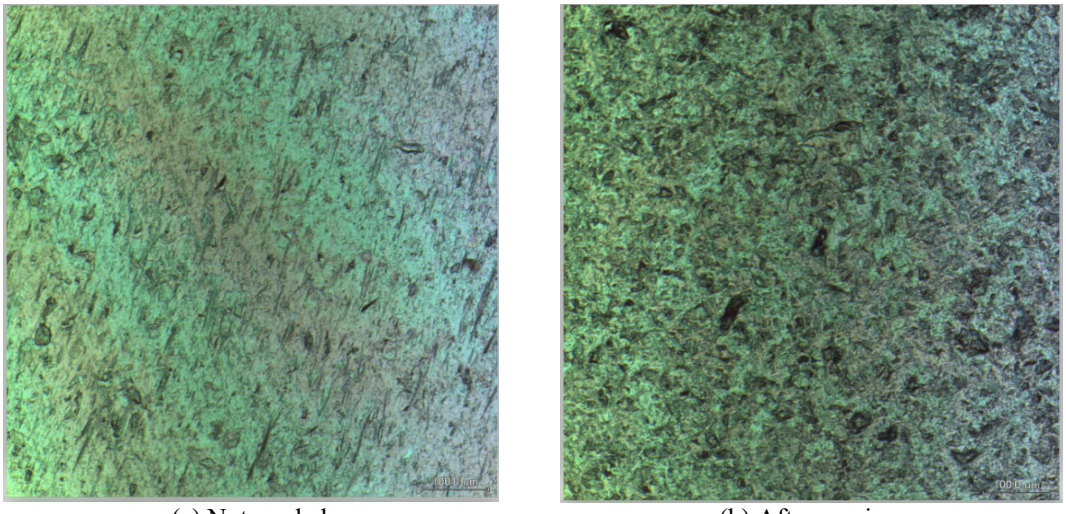

(a) Not eroded (b) After erosion

Figure 23. Comparison of surface morphology of 304 stainless steel specimens before and after erosion

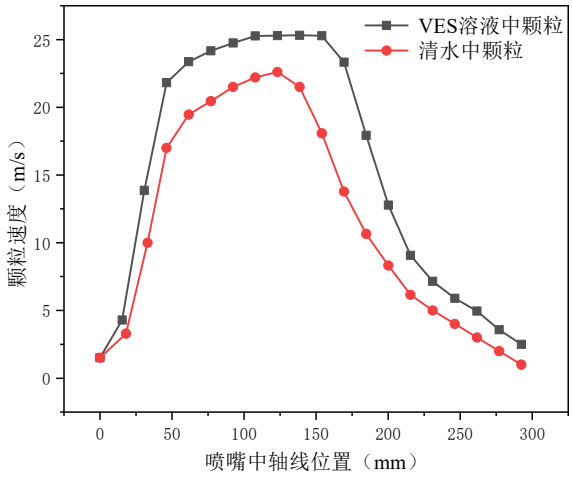

Figure 24. Particle velocity trend at nozzle axis

The data collection of the area impacted by the abrasive particles using a true colour confocal microscope shows the trend of the erosion craters as shown in Figure 25. Comparing the erosion craters of the specimens by water and VES solution respectively, it can be seen that the particles in VES solution obviously impacted the specimens to a higher depth compared to the erosion of the specimens by the particles in water, which also further illustrates that with the turbulent dampening effect of the VES solution, the particles It is also evident that the impact effect of the particles in VES solution is better than that of the particles in water.

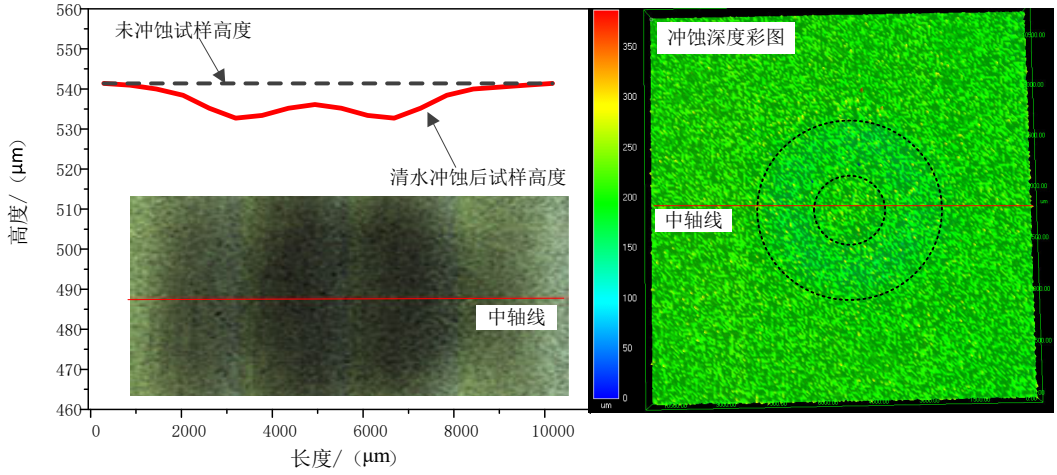

(a) Clear water

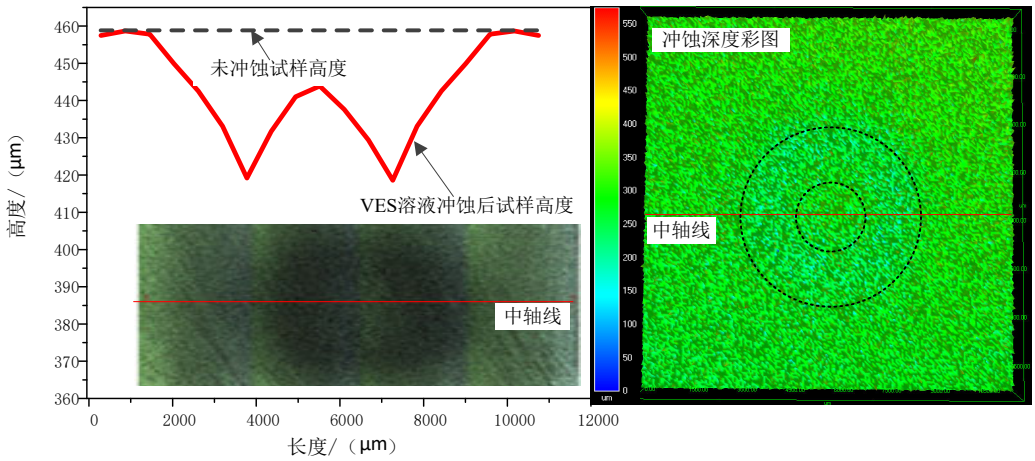

(b) VES solution

Figure 25. Trend in the distribution of specimen erosion crater axes observed by confocal microscopy

5. Conclusion

(1) Comparing the simulation of the jet flow in and out of the nozzle with clear water and Cross fluid, it is concluded that the abrasive follows the particles better in the solution with the addition of drag reducing agent, the velocity difference between fluid and particles is smaller, the particle velocity increases by about 8% and the particles are more

aggregated. Simulation analysis of the jet under different rheological parameters shows that zero shear viscosity η_0 has the most significant effect on the flow field, with the increase of zero shear viscosity η_0 , the velocity of the flow field gradually increases, but the jet agglomeration becomes worse, and the core section of the jet decreases. The optimal rheological parameters are 2.5 Pa-s, -0.1s, and 0.2, respectively, as a result of the orthogonal experimental design of zero shear viscosity η_0 , relaxation time λ_v , and flow index n .

(2) An experimental study was carried out on the optimised streamline nozzle using a submerged erosion test rig to investigate the erosion rate of 304 stainless steel specimens. By comparing the corrosion rate of the specimens with different concentrations of OTAC solution, it can be seen that when the solution is clear water, the corrosion rate of the specimens is the lowest. The addition of 0.2% OTAC with 0.04% nasal to the water resulted in a significant increase in the corrosion rate. At the same time, when the concentration of OTAC was increased, the erosion rate of the specimens increased accordingly. The specimens were scanned using a true colour confocal microscope and the analysis showed that the craters were deeper in the VES solution than in the water, and it was also evident that the crater area was smaller in the VES solution, indicating that the VES solution caused the jets to be more agglomerated.

References

[1] Jiao L F, Li F C. A review of research on additive turbulent drag reduction flow and heat transfer[J]. Advances in Mechanics,2008(03):339-357.

[2] Minghui W, Chenghuai W, Yanxi Z. Numerical Simulation and Experimental Study on Flow of Polymer Aqueous Solution in Porous Jet Nozzle[J]. Advances in Polymer Technology, 2020,2020.

[3] Wang F, Zhou D, Xu Q, et al. Mathematical model of rock stress under abrasive slurry jet impact based on contact mechanics[J]. International Journal of Rock Mechanics and Mining Sciences, 2018,107:1-8.

[4] Li G, Deng S, Guan J, et al. Numerical analysis on cavitation effects in submerged water jet added with turbulent drag-reducing additives [J]. Chemical Engineering Science, 2018, 196.

[5] YANG Shengfa,HUANG Dai,ZENG Shiyu. Effect of ambient flow velocity on the flow field characteristics of abrasive water jets under submerged conditions[J]. Vibration and Shock, 2019, 38(8):7.

[6] Kang Can. Fundamentals and applications of high-pressure water jet technology [M]. Mechanical Industry Press,2016.

[7] Wang Changbin,Shen Yanxia,Liu Zhaodong,et al. Numerical simulation of the submerged abrasive jet field with a tapered straight nozzle[J]. Journal of Daqing Petroleum Institute, 2022(1).

[8] Zhu G, Li H, Wang Z, et al. Semi-resolved CFD-DEM modeling of gas-particle two-phase flow in the micro-abrasive air jet machining [J]. Powder technology, 2021,381:585-600.

[9] Zhang Xueqiang. Design and research of pneumatic conveying device based on EDEM-FLUENT coupling[D]. Xihua University, 2015.

[10] WANG Zhiguo,LIN Jingjie,GUO Jiangru,et al. Numerical simulation of clean fracture fluid proppant placement behavior in fractures based on Cross instantonal equation[J]. Journal of Xi'an University of Petroleum (Natural Science Edition), 2021, 36(03):42-49.

[11] WANG Zhiguo, WANG Shuzhong, SUN Xiao, et al. Microstructure and linear viscoelasticity of OTAC/nasal worm-like micellar fluid[J]. Journal of Mechanics, 2013, 45(6): 7.